Photocrosslinked Co-Assembled Amino Acid Nanoparticles for Controlled Chemo/Photothermal Combined Anticancer Therapy

Tengfei F Wang, Yun Qi, Eijiro Miyako, Alberto Bianco, Cécilia Ménard-Moyon

Photocrosslinked Co-assembled Amino Acid Nanoparticles for Controlled Chemo/photothermal Combined Anticancer Therapy

Tengfei Wang,[a] Yun Qi,[b] Eijiro Miyako,[b] Alberto Bianco,*[a] and Cécilia Ménard-Moyon*[a]*

[a] Dr. T. F. Wang, Dr. A. Bianco, Dr. C. Ménard-Moyon
CNRS, Immunology, Immunopathology and Therapeutic Chemistry, UPR 3572, University of Strasbourg, ISIS, 67000 Strasbourg, France.
E-mail: c.menard@ibmc-cnrs.unistra.fr, a.bianco@ibmc-cnrs.unistra.fr

[b] Y. Qi, Prof. E. Miyako
Graduate School of Advanced Science and Technology, Japan Advanced Institute of Science and Technology, 1-1 Asahidai, Nomi, Ishikawa, 923-1292, Japan.
E-mail: e-miyako@jaist.ac.jp

Keywords: tyrosine, tryptophan, dimerization, tannic acid, self-assembly

Nanostructures formed from the self-assembly of amino acids are promising materials in many fields, especially for biomedical applications. However, their low stability resulting from the weak noncovalent interactions between the amino acid building blocks limits their use. In this work, nanoparticles co-assembled by fluorenylmethoxycarbonyl (Fmoc)-protected tyrosine (Fmoc-Tyr-OH) and tryptophan (Fmoc-Trp-OH) are crosslinked by ultraviolet light irradiation. Two methods are investigated to induce the dimerization of tyrosine, irradiating at 254 nm or at 365 nm in the presence of riboflavin as photo-initiator. For the crosslinking performed at 254 nm, both Fmoc-Tyr-OH and Fmoc-Trp-OH generate dimers. In contrast, only Fmoc-Tyr-OH participates in the riboflavin-mediated dimerization under irradiation at 365 nm. The participation of both amino acids in forming the dimers leads to more stable crosslinked nanoparticles, allowing also to perform further chemical modifications for cancer applications. The anticancer drug doxorubicin (Dox) is adsorbed onto the crosslinked nanoparticles, subsequently coated by a tannic acid-iron complex, endowing the nanoparticles with glutathione-responsiveness and photothermal properties, allowing to control the release of Dox. A remarkable anticancer efficiency is obtained *in vitro* and *in vivo* in tumour-bearing mice thanks to the combined chemo- and photothermal treatment.

1. Introduction

Lessons from Nature brought many inspirations to biomedicine and greatly improved its advances. A typical example concerns the use of natural biomolecules as building blocks to self-assemble into different structures and materials endowed of various functions.[1] Biomolecules are generally more biocompatible compared to artificial and synthetic polymers.[2] Moreover, materials formed from the self-assembly of biomolecules retain some original biological features, which is very important for biomedical applications. Among the wide panel of biomolecules, amino acids, as one class of basic molecules of the living matter, exhibit the capacity of self-assembly.[3] Moreover, they can be easily modified on their amino and carboxylic groups and side chains, allowing to generate a large pool of amino acid derivatives with different functions and properties. Given their excellent biocompatibility and functionalization potential, self-assembled amino acid-based nanomaterials have shown broad prospects for biomedical applications, such as drug delivery, bioimaging and tissue engineering.[4] For example, it was reported that porphyrin-modified diphenylalanine self-assembled into nanodots.[5] The introduction of porphyrin not only facilitated the self-assembly process, but also endowed the nanodots with photothermal properties. Additionally, the co-assembly of porphyrin with Fmoc-$(Leu)_3$-OMe formed nanoparticles that were exploited for photodynamic therapy.[6] However, self-assembled materials driven by noncovalent interactions are generally not stable in some conditions, including physiological environment, acidic and/or basic media and organic solvents, which prevents further modifications and limits their potential in biomedicine.[7] In order to overcome this problem, crosslinking strategies have been developed. A common approach is to use crosslinkers with two reactive terminal moieties, such as aldehyde, amino, carboxyl, azido or alkynyl groups.[8,9] However, the complete removal of crosslinkers from the materials might be difficult, likely causing various problems including cytotoxicity.[10] In this regard, crosslinker-free strategies exploiting particular functional groups in the building blocks presents more advantages. Benefiting from the broad panel of amino acid side chains, self-assembled materials containing amino acids with reactive side chains can be directly crosslinked. For example, the phenol group of tyrosine (Tyr) and the indole group of tryptophan (Trp) can be dimerized through radical reactions.[11] Recently, tyrosine-rich polypeptides have drawn much attention in materials science, showing high potential in forming nanoparticles and hydrogels with various desired features, such as good stability, biocompatibility and fluorescence.[12] Different methods have been developed to form the dityrosine and ditryptophan dipeptides *via* the generation of radicals. For example, peroxidases can oxidize the Tyr side chain and induce the formation of dityrosine.[13] Besides, the UV-

induced crosslinking with or without a photo-initiator can lead to dityrosine or ditryptophan formation.[14] In addition to radical reactions, Tyr can be also crosslinked by a catechol-mediated melanin pathway using the enzyme tyrosinase.[15,16] Covalent bonds can be introduced before or after self-assembly. The former strategy could trigger the self-assembly process, while the latter approach allows stabilizing the nanostructures for further modifications without losing their morphology.[17]

Besides crosslinking, coating strategies can also increase the stability of materials, for instance using polymers. Moreover, the coating can impart to the materials novel properties, such as a photothermal response. Natural polyphenols, like tannic acid (TA) complexed to Fe^{3+}, have drawn much attention for the coating of nanoparticles due to their biocompatibility, stability, stimuli-responsive-degradability, and photothermal and adhesion properties.[18]

Herein, binary amino acid nanoparticles (termed BAP) co-assembled from Fmoc-protected Tyr and Fmoc-protected Trp were crosslinked exploiting the Tyr and/or Trp side chains to increase their stability. Two crosslinking methods using UV irradiation were explored. Different crosslinking compounds, including dimerization and oxidation products, were detected in the crosslinked binary nanoparticles (termed CBP). Next, the stability of the nanoparticles before and after the crosslinking was evaluated under various physical and chemical treatments. Finally, the stabilized CBP were loaded with the anticancer drug Dox and coated by TA/Fe^{3+} complex (termed TAF) for chemo- and photothermal combined anticancer therapy. The TAF coating not only endowed the nanoparticles with photothermal properties, but it also allowed to control the release of Dox inside the cells owing to glutathione (GSH)/pH dual-triggered degradation.[19,20] Aa s consequence, an efficient *in vitro* anticancer effect was observed. These amino acid-based nanoparticles were then exploited *in vivo* in a combined chemo/photothermal therapy (PTT) to treat colorectal cancer.

2. Results and Discussion

2.1 Synthesis and Photocrosslinking of Binary Amino Acid Nanoparticles

BAP were synthesized according to our previous work through the co-assembly of Fmoc-Tyr-OH and Fmoc-Trp-OH in water, which was driven by supramolecular interactions.[21] Due to the weak noncovalent interactions between the amino acids, BAP suffered from a low stability, limiting their applications. In order to improve their stability, a UV-induced-crosslinking was performed to generate covalent bonds into the BAP network (**Figure 1**a). Owing to the Tyr/Trp side chains that can generate radicals under UV light irradiation, a covalent binding between Tyr-Tyr, Trp-Trp and/or Tyr-Trp was expected. Because these aromatic side chains play a

critical role in driving the self-assembly through π-π stacking, their crosslinking would certainly reinforce the nanoparticles. Two photocrosslinking methods applying different UV sources were studied (**Figure S1**). In the first method, we employed a 254-nm light to irradiate the nanoparticles (named CBP_{UV}). In the second method, a 365-nm light irradiation was applied to obtain crosslinked nanoparticles named CBP_{Ribo}. Due to the lower energy of the 365-nm light making Tyr and Trp difficult to be activated, riboflavin (Ribo) was added as a photo-initiator to facilitate the photocrosslinking. The 254-nm light could instead excite the side chain of both Tyr and Trp, and generate radicals due to its strong energy. In contrast, the 365-nm light could excite only Ribo and generate triplet state Ribo (^{3}Ribo) after intersystem crossing. The generated ^{3}Ribo initiated a radical reaction through two different pathways. In type I pathway, ^{3}Ribo directly reacts with the side chains of the amino acids to generate the corresponding radicals. In type II pathway, ^{3}Ribo reacts with triplet O_2 and generates singlet O_2, which has a strong oxidation capacity to produce radicals.[22] The generated Tyr/Trp radicals underwent mainly two competitive routes, namely dimerization and oxidation (**Figure S1**).[11] The dimerization could crosslink BAP, while the oxidation probably helped to increase the water dispersibility of the nanoparticles.

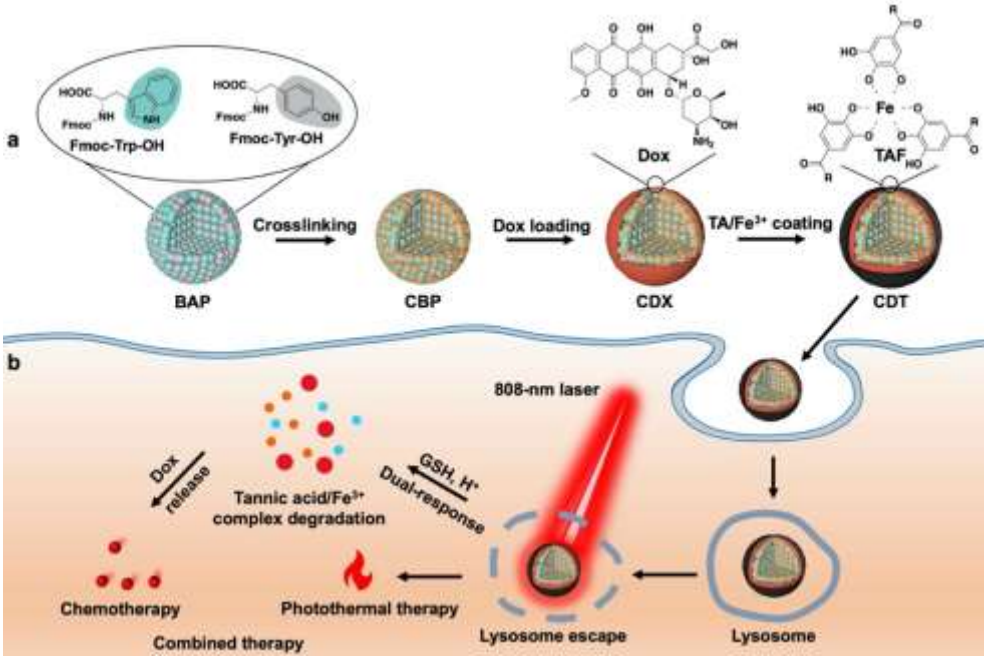

Figure 1. (a) CBP were prepared by the crosslinking of Fmoc-Tyr-OH/Fmoc-Trp-OH co-assembled BAP. Dox was then loaded on CBP through adsorption, followed by TAF coating. (b) TAF coating endowed the nanoparticles with photothermal properties and the capacity of GSH/pH dual-sensitive Dox release, which were exploited for chemo/photothermal combined anticancer therapy.

2.2 Structural and Spectroscopic Characterization of the Nanoparticles

The white colour of the colloidal solution of BAP changed after crosslinking. CBP_{UV} showed a brownish colour and CBP_{Ribo} became yellowish (see insets in **Figure 2**a). The spherical structures were maintained in both cases, as observed in the TEM images (**Figure 2**a), indicating that the photocrosslinking did not alter the morphology of the nanoparticles. The size of the nanoparticles was in the range of 200-300 nm according to the TEM images, in agreement with the dynamic light scattering (DLS) analysis (**Figure 2**b). The polydispersity index (PI) of the nanoparticles was less than 0.2, suggesting a homogeneous size distribution (**Figure 2**b). This was probably due to the highly negative surface of the nanoparticles (zeta potential around -40 mV, **Figure 2**c), which provided sufficient interparticle electrostatic repulsion to prevent their aggregation. After crosslinking, the size of both nanoparticles was slightly increased from ~170 nm to ~250 nm (CBP_{UV}) and ~210 nm (CBP_{Ribo}), and the surface charge was more negative when compared to BAP. These differences were probably caused by photo-oxidation products with more hydroxyl moieties generated during the UV irradiation (**Figure S1**).

Next, we analysed the crosslinked nanoparticles by UV-Vis and fluorescence spectroscopy. An increase of absorbance in the region between 310 and 500 nm was detected in the nanoparticles after the crosslinking, whereas BAP composed of Fmoc-Tyr-OH and Fmoc-Trp-OH had no absorbance from 310 to 800 nm (**Figure 2**d). It has been reported that dityrosine has a specific absorbance band at around 330 nm.[12] The UV irradiation-related products of Trp, including ditryptophan, and their oxidative products absorb between 300 and 500 nm.[23,24] Therefore, the presence of a broad absorbance in both CBP suggested the existence of dimers and oxidized products of the two Fmoc-amino acids. The absorbance of CBP_{UV} above 300 nm was higher and wider than that of CBP_{Ribo} at the same concentration (0.1 mg/mL), indicating a higher crosslinking efficiency for CBP_{UV}, which contained probably more Trp-derived products than CBP_{Ribo}. The nanoparticles were also characterised by fluorescence spectroscopy. As the broad absorbance band in the crosslinked nanoparticles is at 310-500 nm, the nanoparticles were excited at 330 nm wavelength (**Figure 2**e). BAP showed no fluorescence, which can be explained by the absence of absorbance in this region. In contrast, the crosslinked nanoparticles emitted a maximum fluorescence at ~410 nm, with the fluorescence intensity of CBP_{Ribo} higher than that of CBP_{UV}, likely because of dimerization and redox products in CBP_{UV}. Indeed, the lower fluorescence intensity in CBP_{UV} suggested the existence of more oxidized products, which had a broader absorbance and lower fluorescence intensity. When excited at 330 nm, both the dityrosine and the ditryptophan moieties exhibit a fluorescence ranging from 400 to 500 nm wavelength, depending on the substituting groups.[12,23,25] This confirmed the

generation of Fmoc-Tyr-OH and Fmoc-Trp-OH dimers after crosslinking of BAP. Subsequently, the thermal stability of the nanoparticles was studied by thermogravimetric analysis (TGA) performed under inert atmosphere (**Figure 2**f). The residual weight at 900°C was ~13%, 25% and 19% for BAP, CBP_{UV} and CBP_{Ribo}, respectively. The higher amount of residual mass for CBP_{UV} and CBP_{Ribo} compared to BAP was indicative of the generation of compounds with a higher thermal stability after crosslinking, such as oligomers, in particular for CBP_{UV}. Additionally, the TGA curves of Fmoc-Tyr-OH and Fmoc-Trp-OH overlapped before 270°C, indicating the same thermal decomposition behaviour, but a difference was evidenced with the shoulder at around 270-400°C(**Figure 2**g, red frame). Considering the molecular structures of the two Fmoc-amino acids, the only difference is the side chain. We can speculate that the shoulder in the weight loss curves corresponds to the thermal decomposition of the phenol and indole side chains. In both crosslinked groups, the shoulder in this region disappeared, indicating that the side chains changed after the UV irradiation, contrarily to BAP (**Figure 2**f, red frame). The crosslinking clearly enhanced the thermal stability of the nanoparticles by forming dimers, oligomers and oxidised species, with CBP_{UV} containing more high-molecular-weight products than CBP_{Ribo}. Meanwhile, we suggest that the dimerization and the oxidation of Fmoc-Tyr-OH and Fmoc-Trp-OH occurred mainly on their aromatic side chains.

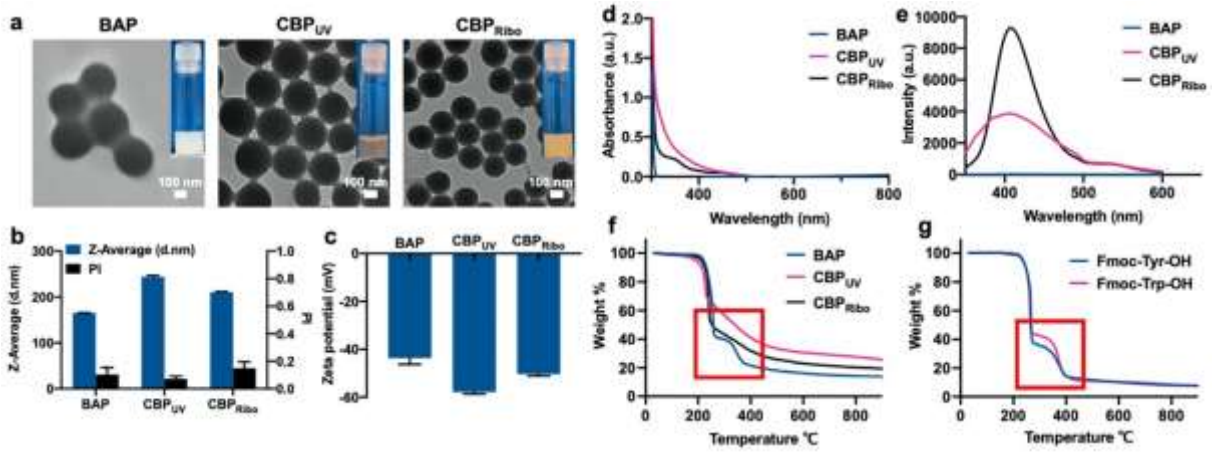

Figure 2. (a) TEM images and photographs of the solutions of the nanoparticles before and after crosslinking. (b) Size and PI assessed by DLS, and (c) surface charge (zeta potential) of the nanoparticles. (d) UV-Vis absorption spectra, and (e) fluorescence spectra of the nanoparticles (excited at 330 nm). (f) TGA of the nanoparticles before and after crosslinking. (g) TGA of the single Fmoc-amino acids.

2.3 Characterization of the Crosslinking Products by High Performance Liquid Chromatography and Liquid Chromatography-Mass Spectrometry

The high-performance liquid chromatography (HPLC) analysis of the BAP group, which contained only Fmoc-Tyr-OH and Fmoc-Trp-OH, showed the peaks of the two compounds, as expected (**Figure 3**a). In the CBP_{UV} group, apart from these two remaining peaks, many new peaks were detected at retention times from ~11.2 to 19.2 min. Moreover, when comparing the ratio of the remaining Fmoc-Tyr-OH and Fmoc-Trp-OH peaks in the BAP group, the peak of Fmoc-Trp-OH decreased more compared to Fmoc-Tyr-OH in the CBP_{UV} group, suggesting a higher reactivity of Fmoc-Trp-OH than Fmoc-Tyr-OH during the crosslinking process. In contrast, in the CBP_{Ribo} group, though there were still new peaks between ~13.8 and 18.4 min, the total area of these new peaks was smaller than that in the CBP_{UV} group, suggesting that fewer crosslinking products were formed. These results confirm the generation of new products after UV crosslinking and highlight differences between the two crosslinked nanoparticles.

Additionally, liquid chromatography-mass spectrometry (LC-MS) was used to identify the crosslinking products in the two types of crosslinked nanoparticles (**Figure 3**b). In the CBP_{UV} group, nearly 90% of the crosslinking products were formed by oxidation of Fmoc-Tyr-OH and Fmoc-Trp-OH, including 60.5% oxidized Fmoc-Trp-OH (Trp-[O]) and 30.6% oxidized Fmoc-Tyr-OH (Tyr-[O]). The higher proportion of Trp-[O] is likely due to a higher oxidation rate constant compared to Tyr.[11] The dimerization-related products accounted for ~10%. Among them, the presence of di-Fmoc-Tyr-OH (Di-Tyr), di-Fmoc-Trp-OH (Di-Trp) and Fmoc-Tyr-OH/Fmoc-Trp-OH dimers (Tyr-Trp) was confirmed, and their proportion was 3.4%, 0.7% and 1.9%, respectively. The UV irradiation generated both Fmoc-Tyr-OH and Fmoc-Trp-OH radicals, and these radicals dimerized mutually. The existence of Tyr-Trp showed that the crosslinking was not only limited to self-dimerization of Fmoc-Tyr-OH and Fmoc-Trp-OH, as the radicals on both Fmoc-Tyr-OH and Fmoc-Trp-OH could also react together. Among the three dimers, the relative amount of Di-Tyr was the highest and that of Di-Trp was the least. The much higher yield of the Tyr-[O] and Trp-[O] indicated that the radical reactions preferentially followed the oxidation pathway in this condition. In addition to Tyr-[O] and Trp-[O], the detection of oxidative dimers (0.9% Di-Tyr-[O], 0.6% Di-Trp-[O] and 1.4% Tyr-Trp-[O]) also supported this conclusion. The higher yield of the oxidation products in CBP_{UV} could mainly result from the generation of reactive oxygen species under 254-nm UV irradiation, which induced the oxidation of the monomers and the dimers. In contrast, in the CBP_{Ribo} group, where the 365-nm UV light was used for the crosslinking, less oxidative products were generated. As shown in **Figure 3**b, 55.2% of the crosslinking products were Di-Tyr, formed in

a much higher proportion than in the CBP_{UV} group. The proportion of oxidative products in CBP_{Ribo} was 44%, including 25.8% Trp-[O] and 17.1% Tyr-[O]. The higher yield of Di-Tyr demonstrated that the use of 365-nm UV and a photo-initiator was more specific for the formation of the Fmoc-Tyr-OH dimer. Moreover, though the Trp-[O] was also detected in CBP_{Ribo}, there were less Trp-related dimers (e.g., Di-Trp and Tyr-Trp). The generation of Trp radicals probably requires a higher energy, and therefore, the irradiation at 365-nm UV yielded less Trp radicals, which mainly underwent photo-oxidation. Overall, by comparing the diversity of the crosslinking products between the CBP_{UV} and CBP_{Ribo} groups, these results indicated that the crosslinking under 254-nm UV light could lead to the generation of more reactive oxygen species and Trp radicals, and thus resulted in more complex reactions. By contrast, the 365-nm UV irradiation with a photo-initiator generated only a limited number of radicals, resulting mainly in the Di-Tyr formation. These differences can also explain their distinct UV-Vis absorbance and fluorescence spectra (**Figure 2**d and e), as well as the different colour of the nanoparticle solutions (**Figure 2**a). Di-Trp and Di-Trp-[O] in the CBP_{UV} group contributed to the broader absorbance band. The brown colour of the nanoparticles was probably due to the indole dimer core in the Trp-related dimers (e.g., Di-Trp and Di-Trp-[O]), which is similar to 5,6-dihydroxyindole polymer, a key intermediate product in the polymerization of dopamine or melanin (**Figure S2**).[26] In the CBP_{Ribo} group, only Fmoc-Tyr-OH participated to the crosslinking, while, both Fmoc-Tyr-OH and Fmoc-Trp-OH jointly formed a covalent network in the CBP_{UV} group. The oxidative products in both CBP_{UV} and CBP_{Ribo} probably correspond to hydroxyl or quinone groups in the aromatic rings, making the surface charge of the crosslinked nanoparticles more negative (**Figure 2**c).

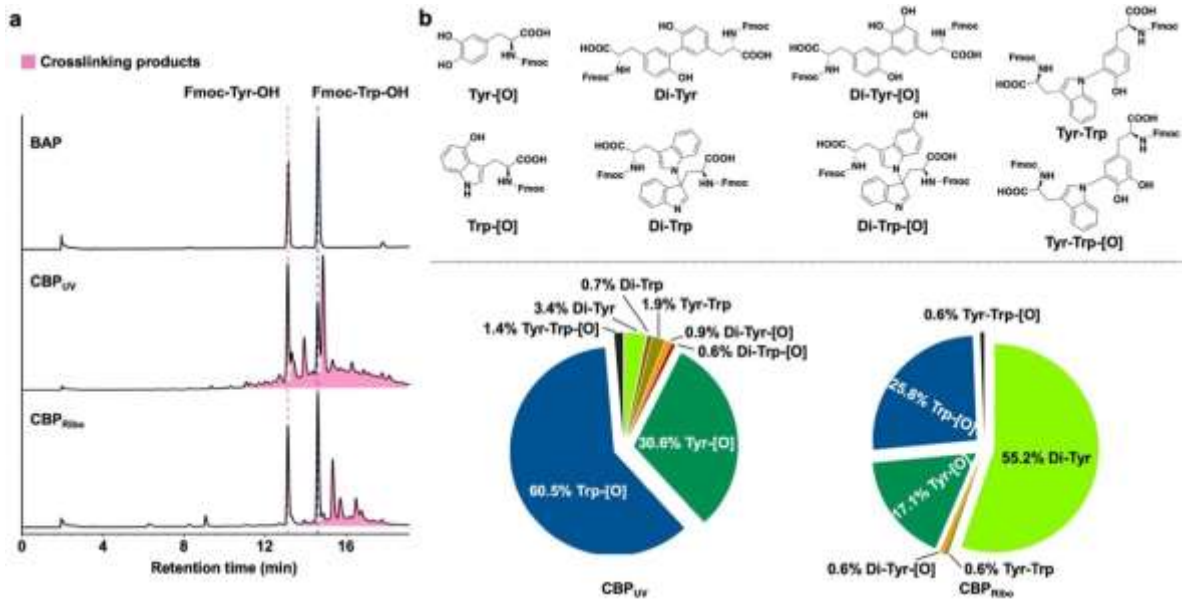

Figure 3. (a) HPLC chromatograms of the nanoparticles before and after crosslinking (detection wavelength: 254 nm). Red and blue dotted lines indicate the position of Fmoc-Tyr-OH and Fmoc-Trp-OH, respectively. Pink areas in the CBP_{UV} and CBP_{Ribo} groups show the crosslinking products. (b) Structures of the possible crosslinking products and their relative percentages in each nanoparticle, identified by LC-MS.

2.4 Stability of the Nanoparticles Before and After Crosslinking

The aim of the crosslinking was to enhance the stability of the nanoparticles, so that they can maintain their structures during the next chemical modification steps. The stability of all nanoparticles before and after crosslinking was evaluated under various physical treatments (e.g., magnetic stirring, washing by centrifugation and resuspension in water, dialysis, and long-time storage) and different chemical environments (e.g., buffers at different pH and cell culture media). The assessment of the Tyndall effect using a laser beam is a fast approach to evaluate the colloidal state of nanoparticle solutions.[27] Any disassembly or aggregation, which disturbs the colloidal state, can influence the laser beam passing through the solutions (Tyndall effect). The untreated BAP, CBP_{UV} and CBP_{Ribo} solutions showed a clear laser beam signal (**Figure S3**). However, this state changed in BAP after the different treatments. Indeed, large aggregates or disassembly/dissolution of the Fmoc-amino acids were observed. In contrast, the crosslinked nanoparticle solutions showed the same Tyndall effect of the untreated groups after the different treatments or after long-time storage, indicating a higher stability due to the introduction of covalent bonds, which contributed to maintain their nanostructures (**Figure 4**).

Apart from the macroscopic observation of the nanoparticle solutions, the state of aggregation or the disassembly was also assessed by DLS. The much higher size and PI values of BAP after

stirring and long-time storage confirmed their aggregation (**Figure S4**a and b). No size and PI results were output in the washed BAP group, which indicated the total disassembly of the nanoparticles. Though no visible aggregation in the BAP solution was observed after dialysis, the DLS analysis showed the presence of a population with ~2 μm size and around 1.0 PI, indicating totally disordered structures. The turbidity of the nanoparticle solutions resulting from their scattering of light also reflected their colloidal state. As shown in **Figure S4**c, the turbidity of BAP decreased after stirring, washing or dialysis, while it increased after storage due to aggregation, confirming their lower stability. On the contrary, the size, PI and turbidity of CBP_{UV} were constant under the different physical treatments (**Figure S4**a, b and c). CBP_{Ribo} were moderately stable, though no difference in their solutions was observed by eye. Their size and PI were nearly unchanged under the various physical treatments (**Figure S4**a and b). However, their turbidity decreased to some extent after some of the treatments (**Figure S4**c), probably because of the partial disassembly of the nanoparticles or little aggregation, which was invisible to the naked eye.

TEM was used to observe the morphology of the nanoparticles after the different treatments (**Figure S4**d). Large and irregular aggregates were observed in the BAP groups after stirring and after long-time storage, confirming the results of the Tyndall effect, DLS and turbidity experiments. Interestingly, nanofiber-like structures were observed in the dialysed BAP, which was in agreement with the DLS analysis. This was probably due to the disassembly of BAP, Fmoc-Tyr-OH having the capacity to form fibers.[21] In contrast, spherical nanostructures, as homogeneous as the untreated ones, were observed in all CBP_{UV} groups after the different physical treatments. However, the structure of CBP_{Ribo} surprisingly changed into homogeneous hollow spheres, with a similar Tyndall effect and size as CBP_{UV}. Nevertheless, their turbidity decreased because the removal of the core increased the transmitted light and reduced the scattering when compared to CBP_{UV}.

For further applications in biomedicine, it is critical that the nanoparticles remain stable also under different chemical environments, including ionic solutions at different pH and cell culture media with serum. Therefore, the stability of the nanoparticles before and after crosslinking was tested in citrate buffer (pH 5.5), phosphate-buffered saline (PBS, pH 7.4), tris(hydroxymethyl)aminomethane hydrochloride buffer (Tris·HCl buffer, pH 8.5) and Roswell Park Memorial Institute (RPMI) 1640 cell culture medium with 10% serum. BAP immediately totally disassembled upon dropping into these buffers and DLS could not provide any reliable value due to the absence of nanostructures existing in solutions (**Figure S5**a and b). The turbidity of these samples was nil, showing transparent solutions due to complete dissolution

(**Figure S5**c). Similar to the results of the physical treatments, CBP_{UV} showed a high stability, whereas CBP_{Ribo} resulted less stable (**Figure S5**a, b and c). The size of CBP_{Ribo} in the citrate buffer and PBS did not change much, but it increased in the Tris·HCl buffer with a large variability (**Figure S5**a). Besides, the PI of CBP_{Ribo} in PBS and Tris·HCl buffer became larger compared to that of the nanoparticles in the citrate buffer and the untreated nanoparticles (**Figure S5**b). Moreover, the turbidity of CBP_{Ribo} in PBS and Tris·HCl buffer was almost zero (**Figure S5**c). These results revealed that CBP_{Ribo} were unstable in PBS and Tris·HCl buffer, and remained intact only in the acidic citrate buffer.

The structures of the crosslinked nanoparticles after incubation in the different buffers were observed by TEM. Since BAP totally dissolved in the buffers, no structures were found in the TEM images. As shown in Figure S5d, integral nanoparticle structures were observed in CBP_{UV} dispersed in the three buffers. In contrast, broken nanoparticles were observed in CBP_{Ribo} incubated in PBS, while some structures were hemispherical with many holes. Moreover, only some fragments were found in CBP_{Ribo} treated in Tris·HCl buffer, while unchanged nanoparticles were observed in the acidic citrate buffer (**Figure S5**d), consistent with the results from DLS and turbidity.

Finally, the stability of the CBP_{UV} and CBP_{Ribo} nanoparticles was studied in RPMI 1640 with 10% foetal bovine serum (FBS). Both CBP_{UV} and CBP_{Ribo} at 10-min and 24-h incubation showed an increase of their size when compared with the untreated nanoparticles (**Figure S6**a), which was probably due to the adsorption of various proteins (protein corona formation). The turbidity of BAP decreased to 0 within 1 min, suggesting a rapid degradation of the nanoparticles (**Figure S6**c). Similarly, a decrease of the turbidity of CBP_{Ribo} was observed within 5 min. The turbidity of CBP_{UV} decreased to 60% in the first 10 min and reached ~30% after 24-h incubation (**Figure S6**c). The structure of the crosslinked nanoparticles after incubation in cell culture medium was observed by TEM (**Figure S5**e). Interestingly, though the turbidity of CBP_{UV} decreased significantly after incubation, the nanoparticles looked unaffected. Moreover, CBP_{UV} after the cell culture medium treatment showed a less contrasted surface, likely because of the adhesion of proteins. In the case of CBP_{Ribo}, hollow structures were observed already after 10 min, and no structures could be found in the TEM images after 24 h. These results confirmed that CBP_{UV} were more stable than CBP_{Ribo} in the cell culture medium, thus being more suitable for their use as drug delivery carriers. Their stability over 30 days was also explored in water, buffers with different pH and cell culture medium (**Figure S7**). The size and PI of CBP_{UV} in these conditions were measured by DLS, and negligible changes were observed, indicating their good long-term stability (**Figure S7a** and **b**). Only the surface

charge of CBP_{UV} was changed from ~-35 mV to ~-20 mV after 30 days in water (**Figure S7c**), but their dispersibility was still satisfactory.

These results showed that CBP_{UV} and CBP_{Ribo} were more stable compared to BAP because of the formation of covalent bonds induced by the photocrosslinking reaction (**Figure 4**). Though LC-MS results demonstrated that CBP_{Ribo} contained a higher proportion of Di-Tyr (**Figure 3**b), the proportion of crosslinked products was lower than that in the CBP_{UV} groups (**Figure 3**a). For CBP_{Ribo}, only Fmoc-Tyr-OH dimerized, while Fmoc-Trp-OH almost did not react, resulting in a less efficient crosslinking (**Figure 4**). Moreover, CBP_{Ribo} with a core-shell structure were observed after physical treatment or incubation in medium, indicating the disassembly of the core, likely due to less penetration of light that only triggered the crosslinking of the amino acids on the nanoparticle surface. In the case of CBP_{UV}, more crosslinked molecules were generated, and both Fmoc-Tyr-OH and Fmoc-Trp-OH participated in the crosslinking, thus imparting a higher stability to the nanoparticles (**Figure 4**). Moreover, the oxidation of CBP_{Ribo} and CBP_{UV} led to the formation of hydroxyl groups on the surface, preventing them from aggregation in water (**Figure 3b** and **Figure 4**). For these reasons, CBP_{UV} were used in the rest of the study (for sake of simplicity, CBP_{UV} are named CBP in the following sections).

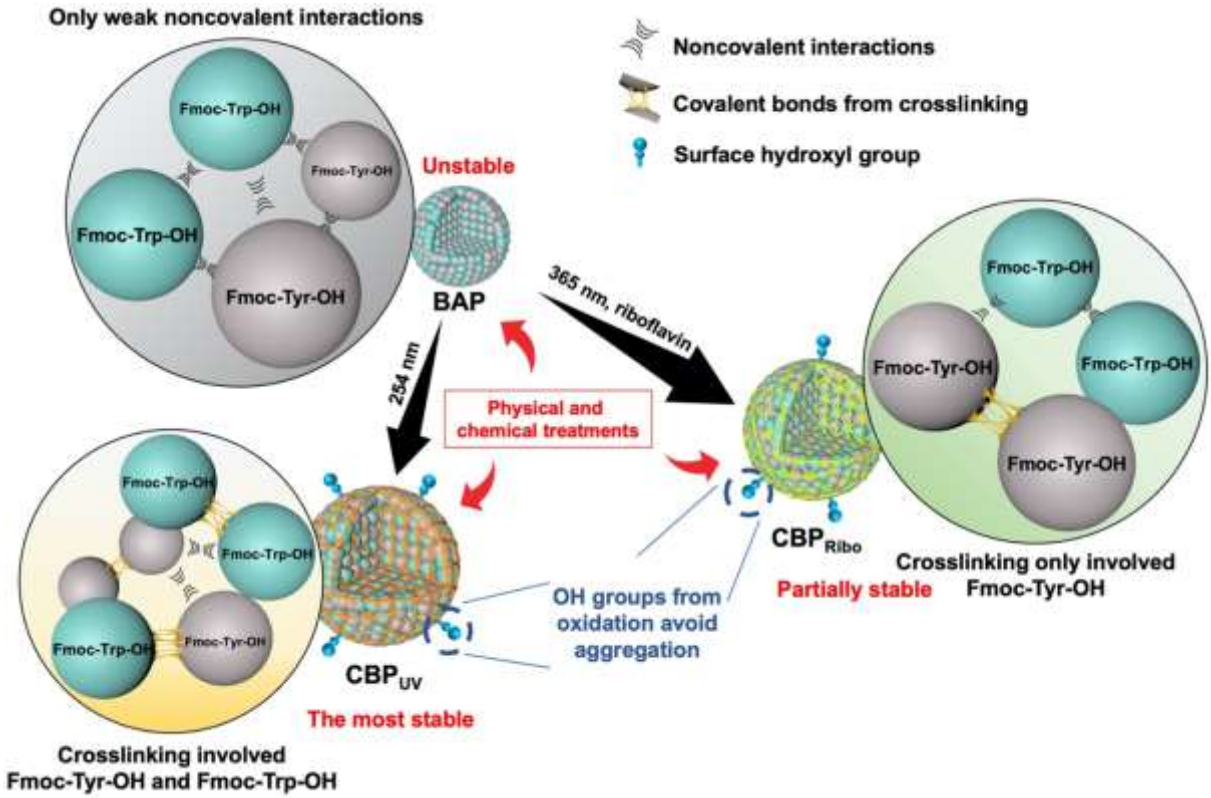

Figure 4. Proposed mechanism explaining the stability of BAP, CBP_{Ribo} and CBP_{UV}.

2.5 Functionalization of CBP with Doxorubicin and Tannic Acid/Fe^{3+} Complex

CBP with enhanced stability, spherical structure and appropriate size showed the potential as nanocarriers for drug delivery. Due to the insufficient anticancer effect of a single therapy, combined chemo- and photothermal therapies with a higher efficiency was designed, allowing to reduce the drug dosage, minimize side effects, overcome multidrug resistance in cancer cells, and eventually improve the overall therapeutic efficacy.[28,29] Firstly, Dox was adsorbed onto CBP thanks to π-π stacking and electrostatic interactions, generating CDX (C: CBP and DX: Dox) (**Figure 1**a). Then, to avoid undesired drug leakage, CDX were subsequently coated with TAF through the formation of coordination bonds between the polyphenol groups of TA, adsorbed on the CDX surface via π-π stacking, and Fe^{3+} ions, generating CDT (C: CBP; D: Dox and T: TAF coating) (**Figure 1**a). The TAF coating endowed the nanoparticles with not only photothermal properties when irradiated by a near-infrared light, but also acid/GSH responsiveness to control the Dox release. Based on this, the multifunctional CDT were constructed with chemo/photothermal anticancer properties and controlled drug release.

Due to the good solubility of the nanoparticles in organic solvents, the amount of Dox loaded in CDX was assessed by HPLC after dissolution in dimethyl sulfoxide (**Figure S8**a). The encapsulation efficiency (EE) and drug loading efficiency (LE) were calculated based on the integration of the HPLC peaks and equation 1 and 2 (see SI, Dox loading section) As shown in Figure S8b, increasing the initial Dox concentration from 0.02 to 0.10 mg/mL, EE decreased from ~85% to ~44%, but LE changed from ~10% to 15%. When the initial concentration of Dox was more than 0.08 mg/mL, the LE remained constant, indicating a loading saturation. As a result, the optimal loading condition was 0.10 mg/mL of Dox, where EE and LE corresponded to 44% and 15%, respectively.

The coating process was optimized to achieve a balance between imparting a significant photothermal capacity, preserving the structure and allowing a sufficient Dox release (**Figure 1**b). For this purpose, we investigated the impact of the ratio and addition sequence of TA and Fe^{3+}, and the thickness of the coating.[30,31] For simplicity reasons, CBP without Dox were used and different conditions were investigated to prepare the TAF-coated CBP (named CTF, C: CBP and TF: TAF coating) (**Table S1**). Their size, PI and surface charge were assessed by DLS. The PI was less than 0.15 in all groups, suggesting that CTF were homogeneous (**Figure S9**a-c). Large size nanoparticles (400-450 nm) were measured when the TA concentration and Fe^{3+} proportion were increased, indicating the generation of a thick layer (**Figure S9**a and b). The size of CTF-Fe-TA (prepared by adding 1.2 mg/mL of Fe^{3+} in CTF solution followed by 0.6 mg/mL of TA, **Table S1**) was similar to that of CBP (~300 nm), probably due to the formation

of a thin layer (**Figure S9**c). In the case of CTF-0.6-2 layers prepared by a multi-layered coating strategy (0.6 mg/mL of TA and 1.2 mg/mL of Fe^{3+}; coating performed twice, **Table S1**), the increase of the size was around 120 nm, indicating that the thickness of the coating was about 60 nm (**Figure S9**c). The zeta potential of all CTF was around -40 mV. The high negative charge surface was likely due to the presence of abundant phenolic hydroxyl groups in TA, ensuring a high water dispersibility of the nanoparticles (**Figure S9**d-f). CTF were then observed by TEM. When the concentration of TA increased, the CTF surface became more and more rough (**Figure S10**a), while it became gradually smoother when the proportion of Fe^{3+} increased (**Figure S10**b). Nevertheless, the surface became rough again in CTF-0.6-2 layers (**Figure S10**c). The rough surface confirmed the coating of the nanoparticles with the TAF complex and the roughness level depended on the coating thickness and Fe^{3+} proportion.

The amount of iron in the different CTF was determined by X-ray photoelectron spectroscopy (XPS) (**Figure S11**). The amount of Fe was consistent with the thickness of the coating, as a higher percentage of Fe atoms was detected in the groups with a thick coating (**Figure S11**a-c). In CTF-0.6-2 layers the amount was 1.8%. XPS survey and high-resolution spectra of CTF showed the presence of the Fe 2p peaks in CTF (**Figure S11**d and e). The position of the Fe $2p_{1/2}$ (725 eV) and Fe $2p_{3/2}$ (712 eV) in the high-resolution spectra confirmed that only Fe^{3+} was present in CTF, whereas no trace of Fe^{2+} was detected (Fe $2p_{1/2}$ expected at 723 eV and Fe $2p_{3/2}$ at 709 eV) (**Figure S11**e).[32] CTF were also characterised by UV-Vis spectroscopy (**Figure S12**). After the TAF coating, the colour of the nanoparticles dispersed in water changed from brownish to dark grey/black. When the concentration of TA increased, the absorbance at 800 nm raised (**Figure S12**a). For different ratios of TA/Fe^{3+}, the absorbance at 800 nm increased when using a higher proportion of Fe^{3+} (**Figure S12**b). Besides, the absorbance of CTF-0.6-2 layers at 800 nm was higher than that of CTF-0.6-1 layer, confirming the importance of the two-step coating process (**Figure S12**c). However, in the case of CTF-Fe-TA, the absorbance at 800 nm was similar to that of CBP (**Figure S12**c). Interestingly, the addition sequence of TA and Fe^{3+} had a clear influence on the formation of the coating. The initial addition of Fe^{3+} led to a negligible TAF coating of CBP. In summary, increasing the TA concentration and Fe^{3+} proportion generated a thicker layer on CBP with a higher absorbance at 800 nm. Finally, the photothermal capacity of CTF was assessed (**Figure S13**). Water and CBP were used as controls. The enhancement of the photothermal performance in the different CTF groups was in agreement with the thickness of the coating and the absorbance at 800 nm. The increase of the temperature was 13.9°C in CTF-0.2/0.1, while it raised to 23.9°C in CTF-0.6/0.3 (**Figure S13**a). The temperature increases for CTF with different Fe^{3+} proportions (CTF-0.6-1/0.5 and

CTF-0.6-1/2) was 24°C (**Figure S13**b), indicating that there was nearly no influence of the TA/Fe^{3+} ratio on the photothermal performance when the amount of TAF coating was high enough. As expected, because of the thin coating, the photothermal capacity of CTF-Fe-TA was very low (**Figure S13**c). However, the photothermal capacity was further improved by forming a multi-layered coating. Indeed, the temperature increase of CTF-0.6-2 layers reached 31.5°C. Next, the influence of the concentration of the nanoparticles and irradiation power was studied using the most efficient system (CTF-0.6-2 layers), showing that the temperature increase was the strongest at the highest concentration and laser power (0.1 mg/mL, 2.0 W/cm^2) (**Figure S13**d). Besides, the photostability of CTF-0.6-2 layers was tested by repeatedly irradiating for 10 min and letting the nanoparticles cooling to room temperature. After three cycles, the same temperature increase was recorded, indicating a stable photothermal performance (**Figure S13**e). Overall, these results confirmed that the thickness of the coating, the roughness of the surface and the photothermal performance were related to the TAF coating conditions. Based on these results, CTF-0.6-2 layers were selected for the rest of the study. Before the biological experiments, the best TAF coating conditions were applied to prepare the nanoparticles loaded with Dox (CDT), which displayed good water dispersibility. TEM allowed to observe spherical structures for CDT, similar to CDX and CTF. As expected, the nanoparticles coated with TAF (CDT and CTF) had a rough surface, in contrast to the smooth surface of CDX (**Figure 5**a). According to DLS, the size of the coated nanoparticles was around 300 nm (PI < 0.2), in agreement with the TEM images and slightly larger than that of CBP (**Figure 5**b). The adsorption of Dox resulted in a less negative charge surface (CDX) when compared with the other nanoparticles coated with TAF (CTF and CDT) or not (CBP) (**Figure 5**c). This is because the adsorption of positively charged Dox neutralized some of the negatively charged groups on the surface of the nanoparticles. The UV-Vis spectra of these nanoparticles were also recorded (**Figure 5**d). A small absorbance was observed at ~490 nm, typical of Dox, in the spectra of CDX and CDT, proving the loading of Dox. The increased absorbance at 800 nm in CTF and CDT confirmed the existence of the TAF coating.

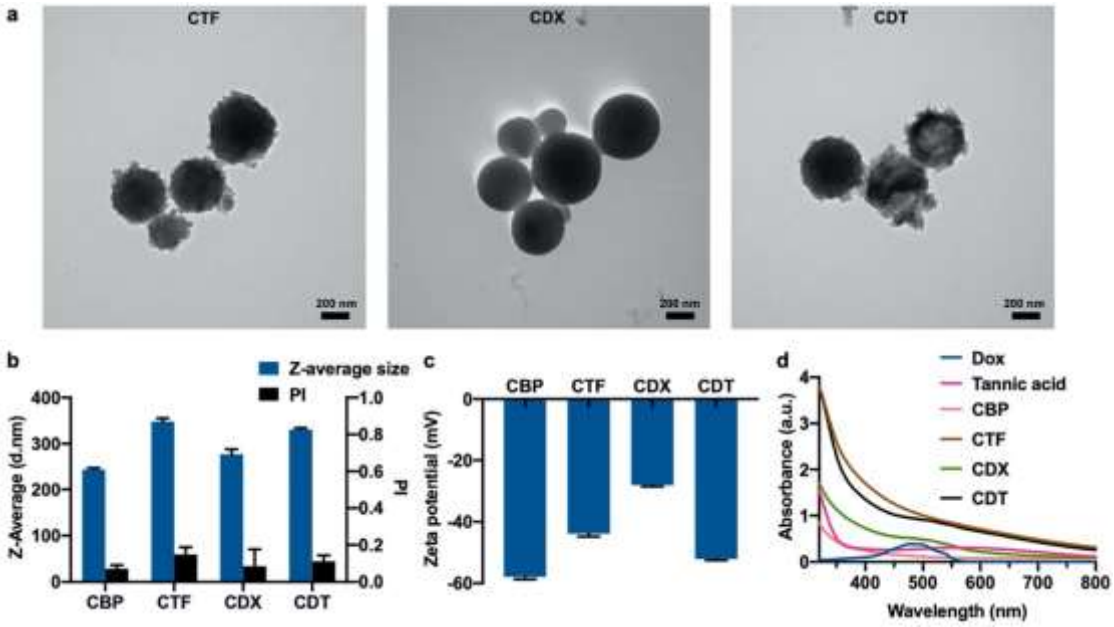

Figure 5. (a) TEM images, (b) size/PI assessed by DLS and (c) surface charge (zeta potential) of CBP, CTF, CDX and CDT. (d) UV-Vis spectra of Dox, TA and the different nanoparticles.

2.6 Glutathione/pH Dual-Responsive Dox Release from CDT

The Dox release from CDT was studied under different physiologically relevant conditions: pH 7.4, pH 5.5 and pH 5.5 with GSH (**Figure S14**a). At pH 7.4, almost no drug was released from CDT, suggesting that the coating was stable at physiological pH, thus preventing the leakage of Dox during the delivery process *in vivo*. Unexpectedly, there was no release of Dox at pH 5.5. Many studies reported the degradation of TAF under acidic conditions, because of the protonation of all the hydroxyl groups, altering the coordination with Fe^{3+}.[33,34] Nevertheless, the decreased absorbance at 800 nm of CDT treated at pH 5.5 evidenced that the acidic environment did affect the coating (**Figure S14**b). We hypothesize that coating of CDT was probably too thick to be fully degraded in slightly acidic conditions over a period of 24 h. When GSH was added to the solution at pH 5.5, the release of Dox was remarkably enhanced (~25% in 24 h) (**Figure S14**a). In our work, we found that GSH induced the degradation of the coating without introducing disulphide bonds, which probably resulted from the competitive binding of GSH and Fe^{3+} to TA, thus breaking the TAF coordination bonds and triggering the Dox release.[18,19] As shown in Figure S14b, the addition of GSH led to a decrease of the absorbance at 800 nm. Moreover, the combined acidic (pH 5.5) and GSH treatment reduced even more the 800-nm absorbance, indicating a significant degradation of the TAF coating. Besides, the change of the colour of the nanoparticle solutions under the different treatments (sole acid, sole GSH and combined GSH/acid) also confirmed the degradation caused by the pH and GSH. The

colour of the dark solutions faded after the sole acid or GSH addition, while an orange/brown solution after GSH/acid combined treatment was observed (**Figure S14**c). The morphology of CDT following the different treatments was monitored by TEM. The GSH-treated CDT showed a less rough surface than the nanoparticles undergoing the acidic treatment, while the surface of CDT treated by acid and GSH was smoother, indicating that GSH enhanced the degradation of the TAF coating more than the acid alone (**Figure S14**d). In addition, XPS was used to detect the oxidation state of the iron ions in CDT after the acid and/or GSH treatment. Not surprisingly, the Fe 2p peaks disappeared after all treatments (**Figure S15**), indicating the GSH/pH dual-responsive degradation of the TAF coating.

2.7 Biocompatibility Study

Besides imparting photothermal capacities and GSH/pH-controlled Dox release, the TAF coating also helped to improve the biocompatibility of the nanoparticles by further enhancing their stability. We investigated the stability of the TAF-coated nanoparticles (CTF and CDT) in RPMI 1640 with 10% FBS. After 24-h incubation, both CTF and CDT maintained their original structures, indicating a good stability in this medium (**Figure S16**a and b). Moreover, the turbidity of CTF in the medium was monitored at different incubation times (**Figure S16**c). A slight decrease to ~85% only happened at the beginning of the incubation (less than 2 h), likely resulting from the slight disturbance of the nanoparticle dispersibility caused by the protein adsorption. After the initial change, the turbidity was constant up to 24 h and there were still ~80% of well-dispersed nanoparticles after 24 h. In order to meet the requirement of biomedical applications, the long-term stability of CDT was also investigated by incubation in water, PBS and cell culture medium for 30 days, and evaluated by DLS. The change of size and PI was negligible over 30 days, suggesting a good stability of CDT. (**Figure S17a** and **b**). Similarly, the zeta potential of CDT in water over 30 days was stable (**Figure S17c**). Moreover, these results were supported by the intact structure of CDT at day 30 as observed under different conditions, confirming their good long-term stability (**Figure S17d**).

Then, we assessed the cytocompatibility of the nanoparticles devoid of Dox (CTF). For this purpose, human breast cancer MCF-7 cell line and human monocytic THP-1-derived macrophages were incubated with different concentrations of CTF and the cell viability was determined by the 3-(4,5-dimethylthiazol-2-yl)-5-(3-carboxymethoxyphenyl)-2-(4-sulfophenyl)-2*H*-tetrazolium (MTS) assay (**Figure 6**a). No significant cell death was found in both cell lines at various concentrations up to 0.15 mg/mL, indicating that CTF had a good biocompatibility. Additionally, the viability of the cells treated by CTF was also evaluated by

the Live/Dead assay (**Figure 6**b). In the Live/Dead assay, live and dead cells can be distinguished by different fluorescence signals using fluorescence microscopy (live cells in green and dead cells in red). Moreover, the fluorescence intensity is correlated with the amount of each type of cells, and thus the cell viability can be measured by microplate reader (**Figure S18**). The viability slightly decreased in both types of cells when the concentrations of CTF reached 0.125 mg/mL, but still ~80% of cells were alive. By the Live/Dead staining, almost no dead cells were found in both MCF-7 cells and THP-1-derived macrophages incubated with the different CTF concentrations (**Figure 6**c). These results showed that CTF induced no significant cytotoxic effects in cancer and immune cells.

Besides the cytotoxicity, the immune response of the nanoparticles was also considered. Except for specific therapies like anti-/pro-inflammatory or cancer immunotherapy, administered therapeutic particles are seen by our immune cells as exogenous matters, thus leading to immune cell activation and cytokine secretion. To evaluate the impact of CTF on immune cells, the level of pro-inflammatory cytokines, including interleukin-6 (IL-6) and tumour necrosis factor-α (TNF-α), secreted from the THP-1-derived macrophages treated with CTF was measured. IL-6 can induce the differentiation of B lymphocytes into plasma cells, which can release antibodies.[35] TNF-α, as one of major regulators, can be rapidly released by macrophages after infection or exposure to exogenous matters, to activate an inflammatory reaction.[36] After incubating the macrophages with different concentrations of CTF, the secretion level of IL-6 and TNF-α showed no significant differences compared to the control (**Figure 6**d and e). Though the secretion of TNF-α was slightly increased at the highest concentrations (0.15 and 0.20 mg/mL), the values were not significantly different and much lower than the positive control, indicating negligible inflammatory responses. These results confirmed the low impact of CTF on immune cells, likely triggering no inflammation during drug delivery.

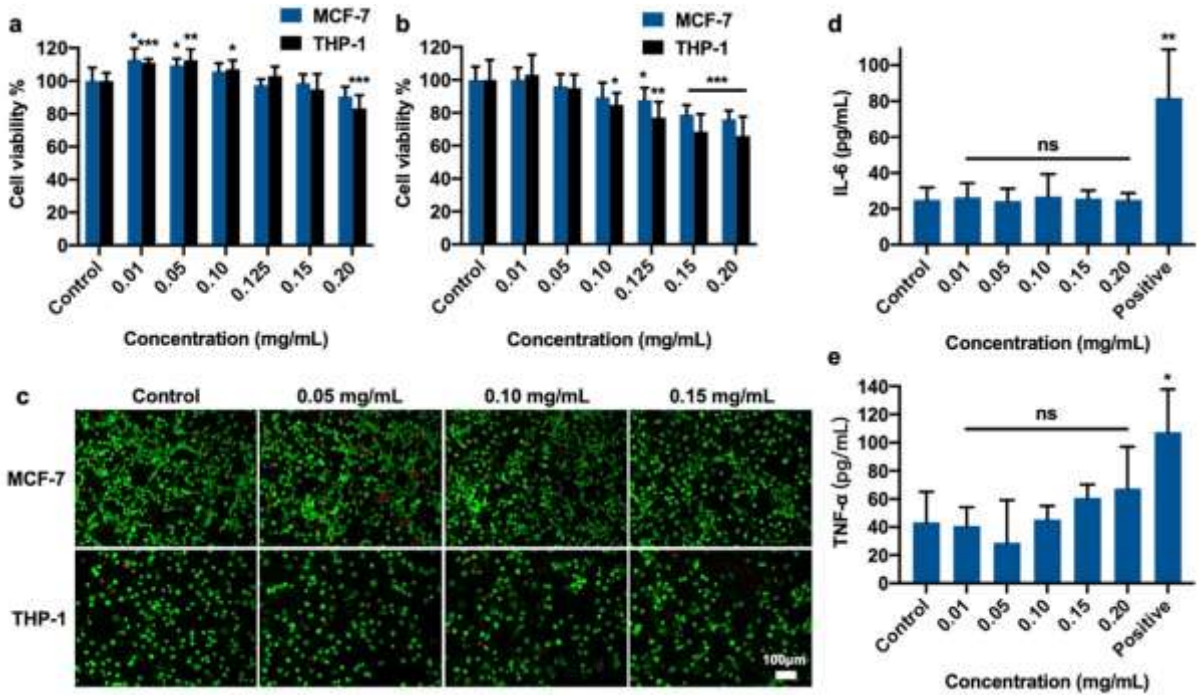

Figure 6. Biocompatibility evaluation of CTF using MCF-7 cell line and THP-1-derived macrophages. Viability of MCF-7 cells and THP-1-derived macrophages incubated with CTF at different concentrations using (a) MTS and (b) Live/Dead assay. (c) Fluorescence microscopy images of the MCF-7 cells and THP-1-derived macrophages treated with CTF and stained by the Live/Dead reagents. (d-e) Secretion of (d) IL-6 and (e) TNF-α by the THP-1-derived macrophages after treatment with different concentrations of CTF. ($p < 0.01$: *; $p < 0.001$: **; $p < 0.0001$: ***).

2.8 Cellular Uptake of CDT

The cellular uptake of CDT was studied by laser confocal scanning microscopy (LCSM). MCF-7 cells were incubated with 0.1 mg/mL of CDT at different time points. Thanks to the intrinsic fluorescence of Dox, CDT were detected by excitation at 488 nm without extra labelling. As shown in **Figure 7**, the signal of Dox (in green) was observed at all three different times (8, 16 and 24 h), and the fluorescence intensity was higher at longer incubation times, indicating the uptake of CDT by the cells. Additionally, because of the GSH-induced intracellular degradation of the TAF coating, the release of Dox could explain the increase in the fluorescence intensity over time. Additionally, the internalization of CDT was also confirmed by flow cytometry. The fluorescence of Dox was detected in the cells in a time-dependent manner, indicating CDT were taken up by the cells (**Figure S19a**). A quantitative analysis revealed a 4-fold increase of the mean fluorescence in the CDT-treated groups compared to the non-treated control. Besides, a 24-h incubation led to a higher internalization of CDT according to the significantly higher

fluorescence compared to 8-h and 16-h incubation (**Figure S19b**). Collectively, these results confirmed the time-dependent internalization of CDT.

Besides, magnified LCSM images showed the subcellular distribution of Dox (**Figure S20**a). By comparing the intensity of the green fluorescence in the nucleus (within the white dash frames) and the cytoplasm (within yellow solid frames), a change of the fluorescence intensity was observed. At 8 h, the fluorescence in the cytoplasm was brighter than that in the nucleus, indicating that most CDT containing Dox were located in the cytoplasm. However, at 16 and 24 h, more and more Dox was observed in the nuclei. Especially at 24 h, the fluorescence was brighter than that in the cytoplasm, suggesting that Dox was mostly concentrated in the nuclei. From the merged images, an orange colour was observed in the nuclei at 24 h, resulting from the colocation of DAPI and Dox, while the nucleus at 8 h was only red. These results confirmed the release of Dox from CDT after cellular uptake and the translocation of Dox into the nuclei over time. Moreover, we saw that the nucleus gradually changed from an integral circle with clear edges (8 h) to irregular shapes at 24 h (**Figure S20**a). This change indicated that the cells started to suffer from apoptosis. We assessed the mean fluorescence intensity by ImageJ software for a semiquantitative analysis (**Figure S20**b-d). The higher intensity in the case of the CDT-treated cells compared to the control cells confirmed the uptake of the nanoparticles. Besides, the fluorescence intensity of Dox increased with longer incubation times, suggesting a continuous uptake of CDT and intracellular release of Dox (**Figure S20**b and c). Additionally, the mean fluorescence intensity in the nucleus and the cytoplasm at different incubation times was compared (**Figure S20**d). At 8 h, the fluorescence intensity in the nucleus was less than that in the cytoplasm. However, at 16 h the intensity was similar in the two cellular compartments. Finally, after 24-h incubation, the intensity of Dox in the nucleus was higher than that in the cytoplasm. The increase of the fluorescence intensity in the nucleus demonstrated the release of Dox from CDT and its translocation to the nucleus.

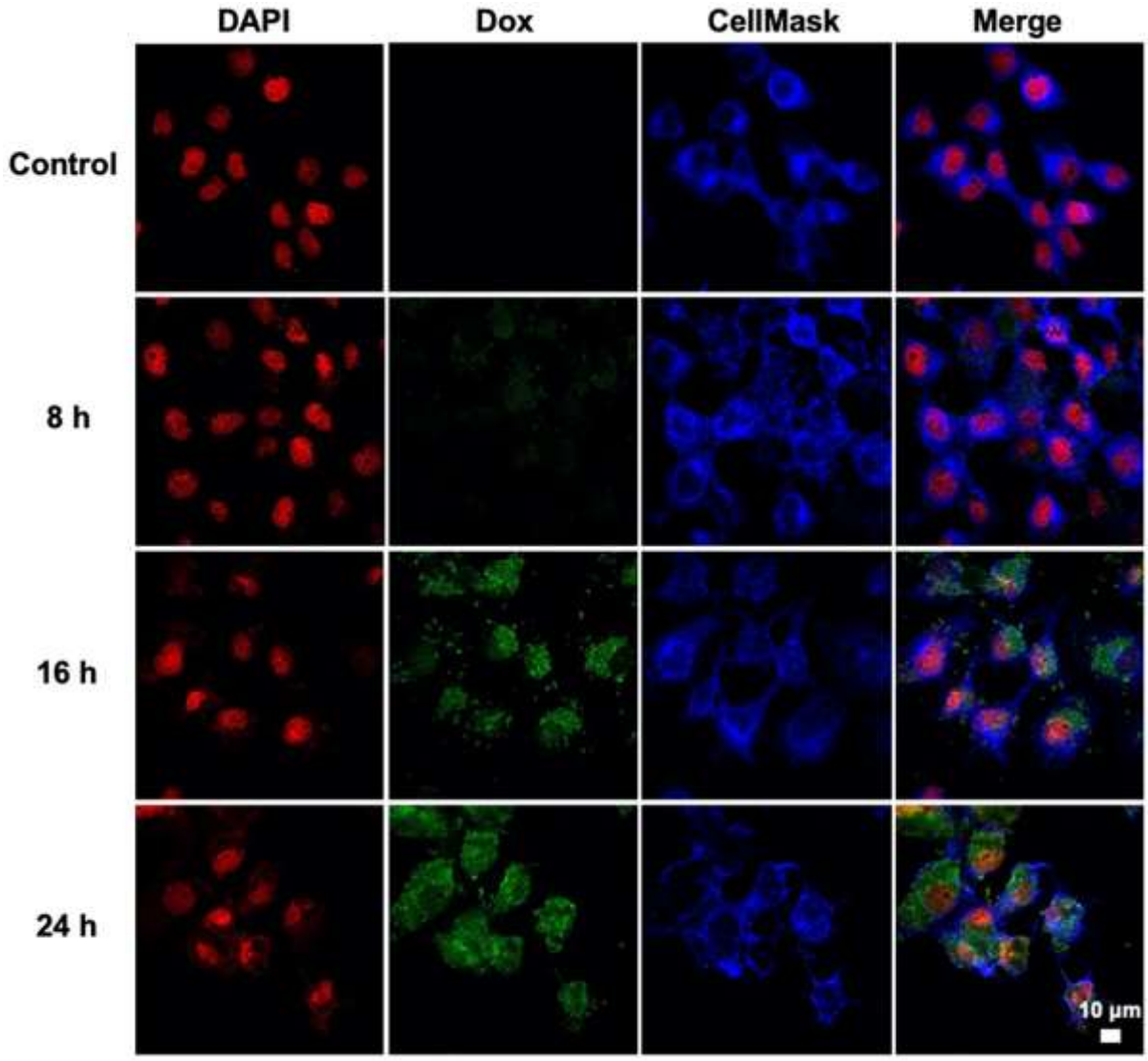

Figure 7. LCSM images of MCF-7 cells treated by CDT at different times. The cell nucleus and plasma membrane were stained with 4',6-diamidino-2-phenylindole (DAPI) in red and CellMask in blue, respectively. The green fluorescence is contributed by Dox.

2.9 *In Vitro* Combined Anticancer Therapy

The potential of CDT for chemo- and photothermal combined anticancer therapy was then evaluated (**Figure 1**b). The chemotherapeutic effect of CDT was first tested. MCF-7 cells were incubated with different concentrations of the nanoparticles for 24 h, and the cell viability was measured by MTS and Live/Dead assays. A concentration-dependent decrease of the cell viability was obtained by both assays from 100 to ~60, ~40 and ~20% at 0, 0.05, 0.10 and 0.20 mg/mL, respectively (**Figure S21**a and b). The fluorescence images of the MCF-7 cells treated by CDT showed that the number of live cells (in green) remarkably decreased, while there were more and more dead cells (in red) with the increase of the CDT concentration (**Figure S21**c). These results showed that CDT displayed chemotherapeutic effect owing to the release of Dox.

Next, we evaluated the anticancer effect of the combined therapy. The MCF-7 cells were incubated for 12 h with 0.05 or 0.10 mg/mL of nanoparticles, then irradiated by 2 W/cm^2 808-nm laser for 10 min and maintained in culture for another 12 h. Control experiments were performed by treating the cells in the same conditions but without irradiation (dark groups). The Dox-free CTF nanoparticles were also used to evaluate the photothermal effect alone. The changes of viability in the CTF dark groups were non-significant compared with control, while a significant cell viability decrease, as assessed by the MTS and Live/Dead assays, was observed in all treated groups under 808-nm irradiation, confirming that the nanoparticles were efficient photothermal agents (**Figure 8**a and b). The viability of the cells incubated with CDT at 0.05 mg/mL with and without irradiation was ~55% and ~35%, respectively, and further decreased to ~40% and ~10% when CDT concentration increased to 0.10 mg/mL. The higher mortality of the MCF-7 cells treated by CDT compared to CTF under the 808-nm laser irradiation indicated that the chemo/photothermal combined therapy was more efficient than the single treatments. Besides killing cells, PTT could also facilitate the lysosomal escape of nanoparticles, promoting chemotherapy.[37,38] The same conclusion was made analysing the fluorescence images through Live/Dead staining. The 808-nm irradiation groups showed less live cells (in green) than the darkness groups, and there were almost no live cells when treated with CDT at 0.10 mg/mL with irradiation (**Figure 8**c).

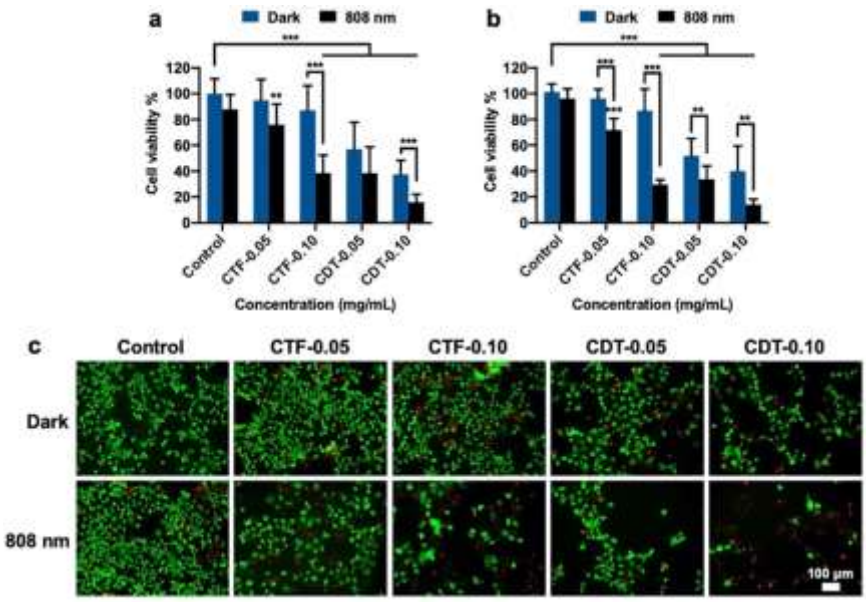

Figure 8. Chemo- and photothermal combined anticancer therapy of CDT. Anticancer effect of CTF and CDT with or without irradiation assessed by (a) MTS and (b) Live/Dead assay. (c) Fluorescence microscopy images of the MCF-7 cells treated by CTF or CDT with or without irradiation and stained by the Live/Dead reagents. ($p < 0.01$: *; $p < 0.001$: **; $p < 0.0001$: ***).

2.10 *In Vivo* Combined Anticancer Therapy

Based on the promising *in vitro* results, we evaluated their anticancer therapeutic efficiency *in vivo* in a colorectal tumour-bearing mouse model generated by subcutaneous implantation of Colon26 cells. Tumour-bearing BALB/c mice were randomly separated into 6 groups and treated by 100 μL of PBS, 2.5 mg/kg of CTF or CDT (250 μg of CTF or CDT for each injection) through intratumoral injection, when the tumour volumes reached around 100 mm^3. Then, for the three PTT groups, the tumours were irradiated by an 808-nm laser for 5 min every day for 16 days. The groups without laser irradiation were used as controls. The tumour volumes and body weight of the mice were measured every day. The temperature of the tumours following the different treatments was monitored during the PTT treatment. The PBS group showed a slight temperature increase from ~33 to ~40°C in 5 min, while the tumour temperature sharply raised to ~55°C in the CTF and CDT groups, confirming the strong PTT effect of the nanoparticles (**Figure 9a and S22**a). We could also confirm the consistent temperature increase around 55°C by using thermographic camera every time when the CTF- or CDT-administered mice were irradiated by the 808-nm laser for 5 min. Therefore, the photothermal stability of the synthesized CTF and CDT were sufficient in the body of the living mice at least 16 days to ensure the effective therapeutic performances of these functional nanoparticles.

Immunohistochemistry (IHC) images from the tumour slices stained by a caspase-3 antibody revealed the anticancer effect of different treatments. Plenty of brownish areas resulting from the release of caspase-3, an initiator of cell apoptosis that can be detected in apoptotic tissues, were observed in the CDT group with laser irradiation, indicating that the combined therapy was able to induce an efficient apoptotic process (**Figure 9**b).[39] The detected caspase-3 in the CTF group with irradiation and in the CDT group without irradiation was lower than the combined therapy group. In contrast, the non-irradiated CTF and PBS groups showed almost no caspase-3 release. Moreover, a terminal deoxynucleotidyl transferase deoxyuridine triphosphate nick end labelling (TUNEL) assay was also performed to identify apoptotic cells through tagging the 3′-hydroxyl termini of DNA breaking points.[40] Again, most cells in the CDT group with combined therapy were apoptotic. When compared with the PBS and non-irradiated CTF groups, much more apoptotic signals were detected for CTF with irradiation group and the non-irradiated CDT group, but still lower than in the combined therapy group (**Figure S22**b). Next, a hematoxylin and eosin (H&E) staining revealed that the areas of necrotic tissues in the irradiated CDT group were larger than in the irradiated CTF group, confirming again the higher efficiency of the combined therapy (**Figure S22**c). The CDT group without

irradiation also showed some necrotic area due to the anticancer effect of Dox, while the tissues were intact in the other groups.

Given the efficient apoptosis and necrosis induction, a remarkable inhibition of the tumour growth was observed in the CTF and CDT groups with irradiation when compared with the PBS groups and the non-irradiated groups, indicating the powerful photothermal therapy (**Figure 9**c). There was also a slight decrease, but not significant, of the tumour volume in the CDT group without irradiation in comparison to the PBS and the non-irradiated CTF groups, resulting from the chemotherapeutic action of Dox. Moreover, the tumours disappeared in 7 and 10 days in the CDT and CTF group with irradiation, respectively. This difference in time suggested that the combined therapy (chemo/PTT) was more efficient than the single therapy (PTT). The therapeutic effect in each group was also evidenced by the representative tumour images at day 8 (**Figure 9**d). The tumours in the PBS group and the non-irradiated CTF groups continued to grow, reaching a big volume. However, the tumour volume was smaller in the non-irradiated CDT group, due to the anticancer effect of Dox. The tumour was instead negligible and totally disappeared in the CTF and CDT groups with irradiation. Moreover, the wounds in these two groups caused by the PTT were healed at the twentieth day. These results are in agreement with the conclusions obtained from the HIC staining of the tumour slices, and reveal a certain antitumour effect for the single therapy and a more robust chemo/photothermal combined effect. Additionally, the body weight of the mice showed that the mice in all groups gained a little bit of weight during the treatment, indicating no side effects (**Figure S22**d). Although it is relatively difficult to achieve a complete response of the tumours by conventional laser-induced photoresponsive nanomedicines,[41-44] we could successfully realize a complete response of our tumour by the light-activatable amino acid nanoparticles, even if repetitive laser irradiation was required. In addition, frequent dosing is generally necessary for typical anticancer drugs such as programmed cell death-1 (PD-1) and cytotoxic T lymphocyte-associated antigen 4 (CTLA-4) immune checkpoint inhibitors to ensure sufficient therapeutic outcomes even though it was found that they could not achieve total resorption of the tumours in rodent cancer models.[45,46] Our light-driven nanoparticle system applied only a single administration with low dose of nanoparticles (2.5 mg/kg) exerting an excellent anticancer activity.[47] Meanwhile, dark toxicity of a conventional photosensitizer is challenging in laser-based anticancer treatment, especially for photodynamic therapy.[48] The optical properties of our amino acid nanoparticles are fully controllable by a therapeutic low-powered laser while not inducing a dark toxicity, although the proposed method might cause slightly burn of the skin around the tumour by powerful photothermal conversion of laser-induced nanoparticles.

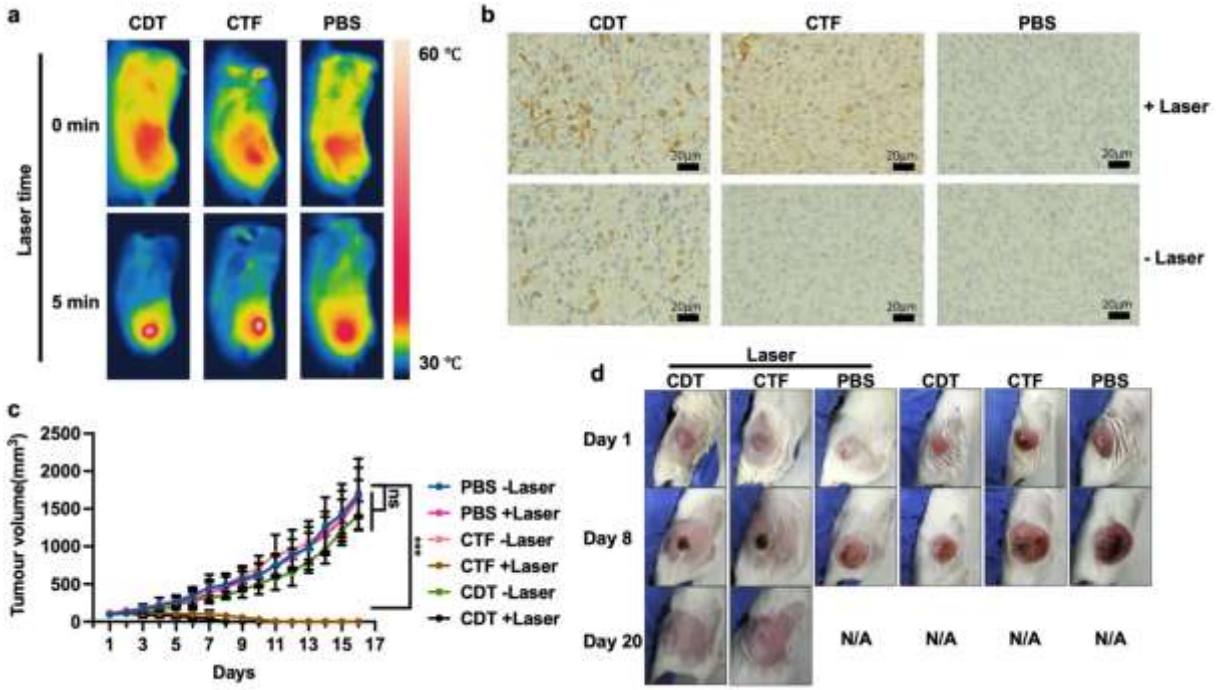

Figure 9. *In vivo* combined anticancer therapy of CTF and CDT. (a) Infrared thermal images of mice treated with PBS, CTF and CDT. (b) Caspase-3 antibody staining of tumour slices after the different treatments. (c) Tumour volume growth curves following the different treatments for 16 days. (d) Representative images of tumours following the different treatments at day 1, 8 and 20. ($p < 0.01$: *; $p < 0.001$: **; $p < 0.0001$: ***).

3. Conclusion

To overcome the issue of low stability of nanoparticles based on the self-assembly of amino acids, which is critical for clinical translation, we formed nanoparticles from the self-assembly of Fmoc-Tyr-OH and Fmoc-Trp-OH (BAP). The nanoparticles were crosslinked by UV irradiation exploiting the side chains of Tyr and Trp to form dimers. Crosslinked nanoparticles showed the same spherical structure as BAP, indicating that the photocrosslinking had no influence on their morphology. CBP_{UV} involved both Fmoc-Tyr-OH and Fmoc-Trp-OH in the dimerization process, while only Fmoc-Tyr-OH participated in the crosslinking in CBP_{Ribo} with a higher proportion of crosslinked products in CBP_{UV}, resulting in a denser covalent network in these nanoparticles and an enhanced stability. CBP_{UV} were modified by the adsorption of Dox and subsequent coating with a tannic acid-Fe^{3+} complex for PTT and GSH/pH-responsive Dox release. Beside the good biocompatibility, we observed an efficient anticancer effect *in vitro* and *in vivo* in response to the combined chemo/photothermal therapy. This work highlights the effective photocrosslinking strategy to overcome the low stability of self-assembled nanoparticles, and shows the importance of controlling the coating conditions to impart

photothermal and drug release capacity to the nanoparticles. The functionalization of the crosslinked nanoparticles is currently being studied to design multifunctional nanoparticles for the treatment of multidrug-resistant cancer.

Supporting Information

Supporting Information is available from the Wiley Online Library or from the author.

Acknowledgements

This work was supported by the Centre National de la Recherche Scientifique (CNRS), by the Agence Nationale de la Recherche (ANR) through the LabEx project Chemistry of Complex Systems (ANR-10-LABX-0026_CSC) and by Jean-Marie Lehn Foundation. E. M. also thanks Japan Society for the Promotion of Science (JSPS) KAKENHI Grant-in-Aid for Scientific Research (A) (Grant number 23H00551), JSPS KAKENHI Grant-in-Aid for Challenging Research (Pioneering) (Grant number 22K18440), the Japan Science and Technology Agency for Adaptable and Seamless Technology Transfer Program through Target-driven R&D (Grant Number JPMJTR22U1), Institute for Fermentation, Osaka (IFO), and the Uehara Memorial Foundation. The authors wish to thank C. Royer from the "Plateforme Imagerie In Vitro de l'ITI Neurostra" CNRS UAR 3156, University of Strasbourg (Strasbourg, France) for TEM observations, C. Antheaume for LC-MS analyses, J.-D. Fauny for confocal microscopy and Y. He for her help with XPS analyses. T. W. is indebted to the Chinese Scholarship Council for supporting his PhD internship.

Conflict of interest

The authors declare no conflict of interest.

References

[1] H. S. Azevedo, I. Pashkuleva, *Adv. Drug Deliv. Rev.* **2015**, *94*, 63.

[2] S. J. Soenen, W. J. Parak, J. Rejman, B. Manshian, *Chem. Rev.* **2015**, *115*, 2109.

[3] K. Tao, A. Levin, L. Adler-Abramovich, E. Gazit, *Chem. Soc. Rev.* **2016**, *45*, 3935.

[4] T. F. Wang, C. Ménard-Moyon, A. Bianco, *Chem. Soc. Rev.* **2022**, *51*, 3535.

[5] Q. L. Zou, M. Abbas, L. Y. Zhao, S. K. Li, G. Z. Shen, X. H. Yan, *J. Am. Chem. Soc.* **2017**, *139*, 1921.

[6] J. L. Li, A. H. Wang, L. Y. Zhao, Q. Q. Dong, M. Y. Wang, H. L. Xu, X. H. Yan, S. Bai, *ACS Appl. Mater. Interfaces* **2018**, *10*, 28420.

[7] M. Diba, G. L. Koons, M. L. Bedell, A. G. Mikos, *Biomaterials* **2021**, *274*, 120871.

[8] O. Barbosa, C. Ortiz, Á. Berenguer-Murcia, R. Torres, R. C. Rodrigues, R. Fernandez-Lafuente, *RSC Adv.* **2014**, *4*, 1583.

[9] M. G. Raucci, M. A. Alvarez-Perez, C. Demitri, D. Giugliano, V. De Benedictis, A. Sannino, L. Ambrosio, *J. Biomed. Mater. Res. A* **2015**, *103*, 2045.

[10] M. Neu, O. Germershaus, M. Behe, T. Kissel, *J. Control Release* **2007**, *124*, 69.

[11] E. Fuentes-Lemus, P. Hägglund, C. López-Alarcón, M. J. Davies, *Molecules* **2022**, *27*, 15.

[12] K. I. Min, G. Yun, Y. Jang, K. R. Kim, Y. H. Ko, H. S. Jang, Y. S. Lee, K. Kim, D. P. Kim, *Angew. Chem. Int. Ed.* **2016**, *55*, 6925.

[13] B. P. Partlow, M. B. Applegate, F. G. Omenetto, D. L. Kaplan, *ACS Biomater. Sci. Eng.* **2016**, *2*, 2108.

[14] K. I. Min, D. H. Kim, H. J. Lee, L. W. Lin, D. P. Kim, *Angew. Chem. Int. Ed.* **2018**, *57*, 5630.

[15] X. K. Ren, Q. L. Zou, C. Q. Yuan, R. Chang, R. R. Xing, X. H. Yan, *Angew. Chem. Int. Ed.* **2019**, *58*, 5872.

[16] A. Körner, J. Pawelek, *Science* **1982**, *217*, 1163.

[17] Y. M. Liu, R. R. Xing, J. B. Li, X. H. Yan, *iScience* **2023**, *26*, 105789.

[18] Y. X. Guo, Q. Sun, F. G. Wu, Y. L. Dai, X. Y. Chen, *Adv. Mater.* **2021**, *33*, 2007356.

[19] S. Kim, S. Philippot, S. Fontanay, R. E. Duval, E. Lamouroux, N. Canilho, A. Pasc, *RSC Adv.* **2015**, *5*, 90550.

[20] Z. H. Guo, W. S. Xie, J. S. Lu, X. X. Guo, J. Z. Xu, W. J. Xu, Y. J. Chi, N. Takuya, H. Wu, L. Y. Zhao, *J. Mater. Chem. B* **2021**, *9*, 4098.

[21] T. F. Wang, C. Ménard-Moyon, A. Bianco, **2023**, under revision.

[22] F. Raiskup, E. Spoerl, *Ocul. Surf.* **2013**, *11*, 65.

[23] S. J. Stachel, R. L. Habeeb, D. L. V. Vranken, *J. Am. Chem. Soc.* **1996**, *118*, 1225.

[24] D. B. Medinas, F. C. Gozzo, L. F. A. Santos, A. H. Iglesias, O. Augusto, *Free Radic. Biol. Med.* **2010**, *49*, 1046.

[25] J. A. Aquilina, J. A. Carver, R. J. W. Truscott, *Biochemistry* **2000**, *39*, 16176.

[26] J. H. Ryu, P. B. Messersmith, H. Lee, *ACS Appl. Mater. Interfaces* **2018**, *10*, 7523.

[27] K. Y. Yan, M. Z. Long, T. K. Zhang, Z. H. Wei, H. N. Chen, S. H. Yang, J. B. Xu, *J. Am. Chem. Soc.* **2015**, *137*, 4460.

[28] J. M. Qin, X. X. Wang, G. J. Fan, Y. N. Lv, J. L. Ma, *Adv. Therap.* **2023**, *6*, 2200218.

[29] W. Q. Bian, Y. K. Wang, Z. X. Pan, N. P. Chen, X. J. Li, W.-L. Wong, X. J. Liu, Y. He, K. Zhang, Y.-J. Lu, *ACS Appl. Nano Mater.* **2021**, *4*, 11353.

[30] X. Zhu, B. G. Guan, Z. L. Sun, X. Tian, X. M. Li, *J. Mater. Chem. B* **2021**, *9*, 6084.

[31] T. Liu, M. K. Zhang, W. L. Liu, X. Zeng, X. L. Song, X. Q. Yang, X. Z. Zhang, J. Feng, *ACS Nano* **2018**, *12*, 3917.

[32] R. J. Tang, C. Jiang, W. H. Qian, J. Jian, X. Zhang, H. Y. Wang, H. Yang, *Sci. Rep.* **2015**, *5*, 13645.

[33] F. B. Hu, R. H. Zhang, W. Guo, T. Yan, X. J. He, F. Z. Hu, F. Z. Ren, X. Y. Ma, J. D. Lei, W. Y. Zheng, *Mol. Pharmaceutics* **2021**, *18*, 2161.

[34] M. A. Rahim, S. L. Kristufek, S. J. Pan, J. J. Richardson, F. Caruso, *Angew. Chem. Int. Ed.* **2019**, *58*, 1904.

[35] O. Dienz, M. Rincon, *Clin. Immunol.* **2009**, *130*, 27.

[36] J. K. Sethi, G. S. Hotamisligil, *Nat. Metab.* **2021**, *3*, 1302.

[37] W. J. Zhang, X. M. Lyu, L. Zhang, W. H. Wang, Q. Shen, S. Y. Lu, L. G. Lu, M. X. Zhan, X. L. Hu, *Macromol. Rapid Commun.* **2022**, *43*, 2100918.

[38] H. Kim, D. Lee, J. Kim, T.-I. Kim, W. J. Kim, *ACS Nano* **2013**, *7*, 6735.

[39] S. McComb, P. K. Chan, A. Guinot, H. Hartmannsdottir, S. Jenni, M. P. Dobay, J. Bourquin, B. C. Bornhauser, *Sci. Adv.* **2019**, *5*, eaau9433.

[40] P. Majtnerová, T. Roušar, *Mol. Biol. Rep.* **2018**, *45*, 1469.

[41] Z. P. Hu, X. M. Li, M. Yuan, X. Y. Wang, Y. P. Zhang, W. Wang, Z. Yuan, *Acta Biomater.* **2019**, *83*, 349.

[42] H. K. Moon, S. H. Lee, H. C. Choi, *ACS Nano* **2009**, *3*, 3707.

[43] C. S. Guo, H. J. Yu, B. Feng, W. D. Gao, M. Yan, Z. W. Zhang, Y. P. Li, S. Q. Liu, *Biomaterials* **2015**, *52*, 407.

[44] B. Zhang, H. F. Wang, S. Shen, X. J. She, W. Shi, J. Chen, Q. Z. Zhang, Y. Hu, Z. Q. Pang, X. G. Jiang, *Biomaterials* **2016**, *79*, 46.

[45] Y. Iwai, M. Ishida, Y. Tanaka, T. Okazaki, T. Honjo, N. Minato, *Proc. Natl. Acad. Sci. USA.* **2002**, *99*, 12293.

[46] Y. Sato, Y. Fu, H. Liu, M. Y. Lee, M. H. Shaw, *BMC Cancer* **2021**, *21*, 1222.

[47] H. Zhang, L. Zhang, Z. B. Cao, S. S. Cheong, C. Boyer, Z. G. Wang, S. L. J. Yun, R. Amal, Z. Gu, *Small* **2022**, *18*, 2200299.

[48] R. R. Allison, K. Moghissi, *Clin. Endosc.* **2013**, *46*, 24.

Photocrosslinked Co-assembled Amino Acid Nanoparticles for Controlled Chemo/photothermal Combined Anticancer Therapy

Tengfei Wang,[a] Yun Qi,[b] Eijiro Miyako,[b] Alberto Bianco,*[a] and Cécilia Ménard-Moyon*[a]*

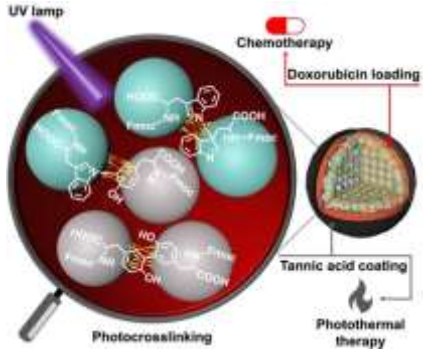

Nanoparticles prepared from the co-assembly of Fmoc-protected tyrosine and Fmoc-protected tryptophan are stabilized using UV-induced crosslinking. After loading doxorubicin on the surface of these nanoparticles, they are coated with a tannic acid/Fe^{3+} complex, to impart photothermal properties and glutathione/pH-responsiveness, allowing to precisely control the drug release. The chemo/photothermal combined anticancer potential of these nanoparticles is evaluated in cancer cells and tumour-bearing mice.